High-Yield Transfer Printing of Metal–Insulator–Metal Nanodiodes

Mario Bareiß,[†,*] Frederik Ante,[‡] Daniel Kälblein,[‡] Gunther Jegert,[†] Christian Jirauschek,[†] Giuseppe Scarpa,[†] Bernhard Fabel,[†] Edward M. Nelson,[§] Gregory Timp,[§] Ute Zschieschang,[‡] Hagen Klauk,[‡] Wolfgang Porod,[§] and Paolo Lugli[†]

[†]Institute for Nanoelectronics, Technische Universität München, Arcisstrasse 21, 80333 Munich, Germany, [‡]Max Planck Institute for Solid State Research, Heisenbergstrasse 1, 70569 Stuttgart, Germany, and [§]Center for Nano Science and Technology, University of Notre Dame, 275 Fitzpatrick, Indiana 46556, United States

ABSTRACT Nanoscale metal–insulator–metal (MIM) diodes represent important devices in the fields of electronic circuits, detectors, communication, and energy, as their cutoff frequencies may extend into the "gap" between the electronic microwave range and the optical long-wave infrared regime. In this paper, we present a nanotransfer printing method, which allows the efficient and simultaneous fabrication of large-scale arrays of MIM nanodiode stacks, thus offering the possibility of low-cost mass production. In previous work, we have demonstrated the successful transfer and electrical characterization of macroscopic structures. Here, we demonstrate for the first time the fabrication of several millions of nanoscale diodes with a single transfer-printing step using a temperature-enhanced process. The electrical characterization of individual MIM nanodiodes was performed using a conductive atomic force microscope (AFM) setup. Our analysis shows that the tunneling current is the dominant conduction mechanism, and the electrical measurement data agree well with experimental data on previously fabricated microscale diodes and numerical simulations.

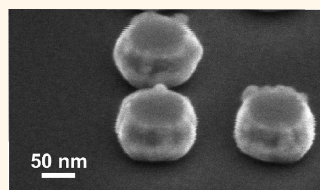

KEYWORDS: metal–insulator–metal nanodiodes · nano transfer printing · terahertz rectifier · conductive atomic force microscope · tunneling current

Metal–insulator–metal (MIM) junctions represent promising devices for various electronic and optoelectronic applications, such as antennas for energy harvesting[1,2] or infrared detection,[3] field-emission cathodes[4] and switching memories.[5] Of particular interest are devices operating at a few THz, a frequency range where sensing[6] and communication[7] are particularly attractive. Other applications of THz devices involve biomedical investigation of DNA[8] or enzymes,[9] or night-vision cameras and security equipment. MIM structures consist of two metal layers separated by a nanometer-sized insulator. Several materials for the insulating layer have been reported, including various oxides.[10–13] In the field of rectennas for infrared detection, native aluminum oxide (AlOx) has been the insulating material of choice so far.[14] However, naturally grown oxides are not very reliable and reproducible even in simultaneously fabricated diodes (see Supporting Information). Here, we present a fabrication method of a ~3.6 nm thick, low-defect AlOx. When applying a high-frequency alternating electrical field across the MIM junction, for example, in the terahertz (THz) regime, tunneling electrons can follow this field as the cutoff frequency of nanoscale MIM structures can reach several hundreds of THz.[15] Because of the nonlinear I–V characteristics of a quantum mechanical tunneling current, the MIM junction can act as a rectifying device.[16] By using two different metals for the contacts, rectification can be achieved at zero bias. So far, only isolated nanoscale MIM diodes containing an air oxidized insulator have been reported.[17] We present here for the first time a high-yield scalable method for the fabrication of several millions of vertical MIM nanodiodes in one single process step, namely a temperature-enhanced nanotransfer printing process. In previous works, various microscopic scale devices have been successfully transfer-printed.[18–21] In particular, we presented recently transfer-printed MIM diodes (MHz rectifiers)[22] which also feature spatial dimensions in the micrometer range. A transfer-printed electrical nanodevice has not been demonstrated so far. A conductive atomic force microscope (C-AFM) setup[23] is used to electrically characterize individual MIM nanodiodes. We demonstrate the functioning of the nanodevices and the fabrication method by comparing the current–voltage characteristics of the printed nanoscale MIM diodes to those of printed microscale diodes, which we previously reported. The diode operation is analyzed by numerical simulations. Finally, the THz performance of the transfer-printed MIM structure is estimated.

* Address correspondence to Bareiss@nano.ei.tum.de.

Received for review January 27, 2012 and accepted March 2, 2012.

Published online March 02, 2012
10.1021/nn3004058

©2012 American Chemical Society

DISCUSSION

Temperature-Enhanced Nanotransfer Printing of MIM Nanodiodes. Electron-beam lithography (EBL)[24,25] is a commonly used method for patterning materials and fabricating devices with dimensions between 30 and 100 nm. However, EBL lacks the fabrication speed and cost efficiency required for the processing of large areas. In contrast, nanotransfer printing (nTP) offers the possibility to print large, dense arrays of nanoscale devices on arbitrary flat surfaces, provided the adhesive and cohesive forces, surface energies, and material properties are properly tailored.[26] Using temperature-enhanced nTP, we have fabricated an array of approximately 4 million MIM pillar diodes, each with a diameter of less than 100 nm, suitable for electronic and optoelectronic applications.

First, a stamp was designed and fabricated from a silicon wafer by EBL and highly anisotropy reactive ion etching (RIE). The stamp contains an array of cylindrical mesas covering a square area of 300 × 300 μm^2 (see Figure 1a for a schematic, and Figure 2a for an electron microscopy image). Successful transfers with stamps up to 1 cm^2 have also been performed. The mesas have a height of 80 nm to provide good physical stability during the printing process. The diameter of the mesas and the spacing between adjacent mesas was designed between 50 and 100 nm.

The preparation of the stamp prior to printing is outlined in Figure 1b−e. First, the stamp was covered with an alkylsilane self-assembled monolayer (SAM) to reduce its surface energy. Next, a 15 nm thick layer of AuPd was deposited by thermal evaporation onto the SAM-covered stamp to provide a delamination layer from which the MIM pillars can later be easily transferred to the target substrate. In the next step, a 25 nm thick layer of aluminum with a surface roughness of less than 1 nm was deposited as the first electrode. The stamp was then briefly exposed to oxygen plasma to form a high-quality aluminum oxide tunnel barrier with a thickness of 3.6 nm.[27] Compared with aluminum oxide obtained by native oxidation in air, the oxygen-plasma-grown oxide has been found to provide substantially better reliability and reproducibility. To complete the MIM structure, a 15 nm thick AuPd layer was then deposited as the second electrode. Finally, a 4 nm thick layer of titanium was deposited by evaporation to provide an adhesion promoter for the nanotransfer printing process. To facilitate good physical contact between the stamp and the target substrate, the layer stack deposited onto the stamp must be as smooth as possible. Therefore, metals with a small grain size, such as Al, AuPd, and Ti, are more desirable than, for example, Au. During the metal evaporations the stamp was held perpendicular to the metal source in order to minimize the deposition of metals on the sidewalls of the mesas (see Figure 2b) and Figure 2c)).

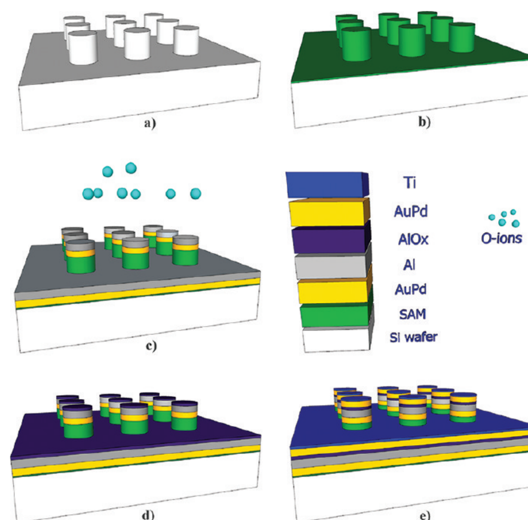

Figure 1. Sequence of process steps to prepare the stamp for transfer-printing of the nanoscale MIM pillars. (a) An array of mesas with a height of 80 nm and a diameter of 50 to 100 nm is fabricated on the surface of the silicon stamp by electron-beam lithography and highly anisotropic silicon etching. (b) The silicon stamp is covered with an alkylsilane self-assembled monolayer (SAM). (c) 15 nm of AuPd and 25 nm of Al (first electrode of the MIM diodes) are deposited by thermal evaporation. (d) The Al surface is exposed to oxygen plasma to form a ~3.6 nm thick AlOx tunnel barrier. (e) Finally, 15 nm of AuPd (second electrode of the MIM diodes) and 4 nm of Ti (to promote adhesion to the target substrate) are deposited by thermal evaporation.

As target substrate we have used a p-type silicon wafer covered with an AuPd layer (to electrically connect the bottom electrodes of all diodes) and a thin titanium layer (to provide good adhesion of the printed layer stack). Immediately prior to printing, the titanium-coated surfaces of the stamp and the target substrate were physically activated (the parameters can be found in the Supporting Information). When the titanium-covered MIM pillars on top of the mesas of the stamp are brought into physical contact with the titanium-covered target substrate, individual and isolated MIM nanodiodes are transferred from the stamp to the substrate, resulting in a high density of devices. The transfer process is facilitated by applying a temperature of 200 °C during printing. We found that such a high temperature promotes the formation of covalent bonds between the titanium layers on the top of the stamp and on the substrate due to the removal of water molecules.[28]

Morphological Characterization of Printed Nanoscale MIM Diodes. To investigate the quality of the nTP process, three nominally identical samples were fabricated and investigated by scanning electron microscopy (SEM). The transfer yield, which we define as the number of properly transferred MIM diode stacks divided by the number of pillars on the stamp, was found to be 98%, which means approximately 4 million diodes were successfully transferred. During the metal and insulator deposition process, material was deposited not only on

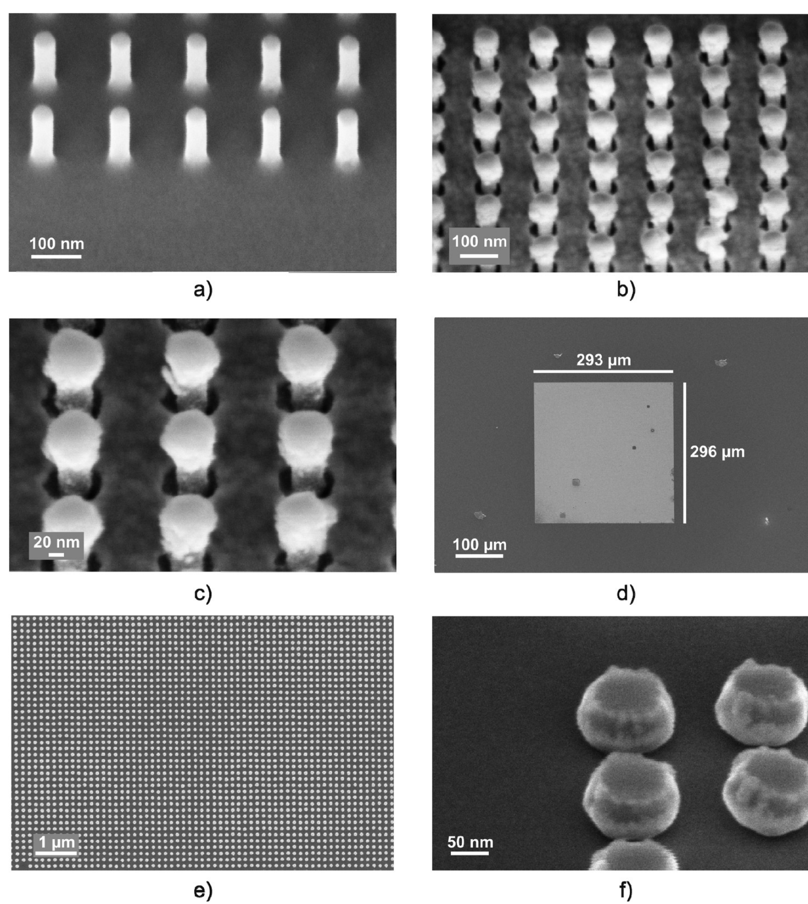

Figure 2. Stamp preparation and large area out-of-plane printed nanodiodes. (a) A scanning electron microscope (SEM) image of an edge of the Si stamp is shown at a tilt angel of 45°. The pillars feature a height of 80 nm and a diameter of 50 nm. (b) Metal layers and an insulator are fabricated on the stamp that is covered with a hydrophobic self-assembled monolayer. (c) No material was deposited on the sidewalls of the pillars as we used collimator plates during the evaporation. (d) After covering the stamp with metals and the insulator, almost the whole array of MIM nanodiodes was transfer-printed on a target substrate. (e) A zoom of the printed area covered with nanodiodes is presented here. (f) 3-Dimensional individual diodes can be seen by tilting the electron beam by 54°. The surface of the printed nanodiodes is very smooth allowing contacting the top with a conductive atomic force microscope.

the top of the pillar structures of the stamp, but also around the periphery of the previously deposited metal stack (although not on the sidewalls of the pillars). Therefore, the area of the MIM structure increases with increasing metal layer thickness. Indeed, the diameter of the transferred quantum devices was found to be larger by about 45 nm than the original feature size on all three stamps. Taking these effects into consideration, the diode area and the distance from each other can be tailored very precisely, and nanoscale structures with a very high density can be fabricated. To compete with high resolution EBL fabrication techniques, the morphology and height of the printed devices have to be homogeneous and must remain unchanged after the printing process. The fidelity of the printing process is proven by the perfect match between the height of the transfer-printed MIM diodes, measured with an atomic force microscope (AFM), and the evaporated material thicknesses on the stamp. The printed quantum pillars have a height of 60 nm and feature a stack shape expected from the original layer depositions on the stamp. The top surfaces of the transferred tunneling diodes are very smooth, thus providing an excellent contact area for electrical characterization with a conductive AFM tip.

We have therefore demonstrated that several millions of MIM nanodiodes can be fabricated by a few evaporation steps and a fast printing process, without need of resists or other patterning steps (other than those used to make the stamp), followed only by some plasma treatments. Thus, temperature-enhanced nTP provides a solution to the challenge of fabricating large-scale and high-density homogeneous arrays of nanoscale devices in a fast and economic way. The stamp can be used several times before degradation occurs.

Electrical Characterization with Conductive AFM Tips and Numerical Simulation. The electrical properties of the transfer-printed MIM nanodiodes have been quantified using a conductive atomic force microscope (C-AFM). With this high spatial resolution characterization method, several nanodiodes have been tested individually, and

the static device parameters of single nanodevices have been extracted, allowing conclusions about the underlying electron transport mechanism. The conductive AFM tips consisted of silicon covered by a Pt–Ti alloy and featured a tip radius of 15 nm. The electrical setup allowed a local application of voltages up to 10 V and measurement of the current at the same time. The sample with the printed rectifiers was placed on a ceramic holder, wherein the AuPd layer on the substrate was connected through a magnetic gold clamp from the top (see Figure 3b). As the AuPd electrode of the printed MIM structure was attached to the conductive metal layer on the substrate, the bottom of the transfer-printed diode was directly connected to the gold clamp. The top of the diode, consisting of the Al and the AuPd delimitation layers, was electrically connected *via* the C-AFM tip. The conductive tip and the gold clamp on the substrate were connected to a parameter analyzer which was located in the head of the C-AFM setup (see Figure 3a). This circuit was used for the electrical characterization of single MIM nanodiodes. The voltage was applied on the C-AFM tip, and the current was measured at the same time.

As the area of the MIM diode is in the nanometer range, currents from 10^{-19} A up to 10^{-6} A are expected. Although the C-AFM setup was in a temperature, humidity, and vibration controlled environment, electrical noise still occurred, and the lowest measurable currents were in the 100 pA-range which is similar to C-AFM measurements reported in literature.[29,30] We investigated several nanodiodes, and only one diode showed a short circuit behavior. In all other diodes, an exponential I–V characteristic was measured (see Figure 4a). An asymmetric tunneling current behavior with respect to the applied bias was observed as expected due to the asymmetric diode structure with different metal electrodes. In a comparison of the measured current density of the nanoscale tunneling diodes with previously transfer-printed diodes featuring an area in the micrometer range,[31] the current densities are in excellent agreement to each other proving the quality of the materials and fabrication process. The electrical stability under an applied voltage was improved by a factor of at least 2 by reducing the area of the tunneling diodes. The previously presented tunneling diodes showed a breakdown behavior around 5 to 6 V. In contrast, the nanoscale diodes worked at least up to 10 V. We believe that the improved break down behavior is related to the reduced number of defects found in the insulating layers as the diode area is scaled down. This is another indication of the high quality of the ultrathin AlOx layer fabricated by the plasma treatment.

To extract static device parameters and to determine whether or not tunneling is the dominant transport mechanism, numerical simulations were carried out.[32] Hole currents can be neglected since the tunnel barrier for holes is much higher than for electrons. By assuming that direct/Fowler-Nordheim tunneling is the dominant tunneling process, the current density can be modeled by the Tsu–Esaki formula:[33]

$$J = \frac{em_e k_B T}{2\pi^2 \hbar^3} \int P(E) \ln\left\{\frac{1+\exp(-E/k_B T)}{1+\exp[-(eV+E)/k_B T]}\right\} dE$$

where $P(E)$ is the transmission coefficient for electrons with energy E. An excellent fit of the simulation for voltages up to 6 V was accomplished when considering an energy dependent effective tunneling mass and using tunnel barrier heights of 4.2 eV for the AuPd electrode and 2.8 eV for the Al electrode. The value of 4.2 eV at the AuPd–AlOx interface corresponds to the barrier height of Au in the Schottky limit. As the barrier height at the Al–AlOx interface is known to be dependent on the growth mechanism, a smaller barrier height of 2.8 eV than the expected value of 3.1 eV can be explained by the formation of a dipole layer produced by charge transfer between the Al electrode and interfacial gap states in the AlOx which is known to reduce the oxide barrier height.[34,35] For higher voltages, the simulation predicts higher values for the current density. However scattering processes like electron–phonon interactions are not included in the simulation which are expected to reduce the tunneling current.[36]

Currently, we are working on a carbon-nanotubes (CNT)/graphene transfer process in order to place a highly conductive film on the top MIM layer for addressing not only single MIM nanodiodes, but an array of diodes.

Estimation of the Nanodiodes Cut-off Frequency. The cut-off frequency (f_{cut}) is the maximum frequency at which an electrical device still works properly.[37] By approximating a nanodiode as a parallel-plate-type capacitor, f_{cut} is defined as

$$f_{cut} = \frac{1}{2\pi RC} = \frac{d}{2\pi R \varepsilon_0 \varepsilon_r A}$$

where R is the resistance of the lead lines (here the external wires and the AuPd substrate), and C is defined by the capacitive area A and dielectric thickness d. Here, the tunnel resistance of the diode can be neglected as it is much higher and in parallel to the resistance of the lead lines.[16] The increase of the thickness of the dielectric leads to an increase of the cutoff frequency. However, the tunneling current is exponentially dependent on the tunnel barrier thickness. Thus, a dramatic current decrease can be expected when increasing the thickness of the dielectric. In general, a direct measurement of the permittivity of MIM nanodiodes is not possible with a C-AFM setup. However, we have previously determined the permittivity of the MIM diodes comprising a microscale area

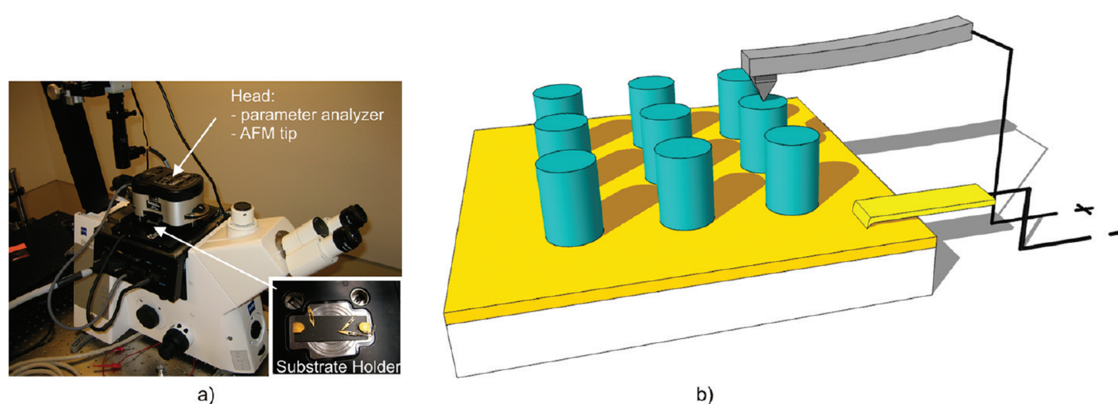

Figure 3. Conductive atomic force microscope setup. (a) A photograph of the conductive atomic force microscope (AFM) setup: The parameter analyzer and the AFM tip are implemented in the head, and the substrate holder comprises ceramic plate and gold clamps for connecting the sample substrate. (b) A schematic view of the AFM setup: The MIM pillars (turquois) that are transfer-printed on a Si wafer (white) comprising a conductive AuPd layer (orange) are contacted from the top *via* a conductive AFM tip (here, positive voltage). The AuPd-layer on the substrate is connected *via* a gold clamp (here, negative voltage).

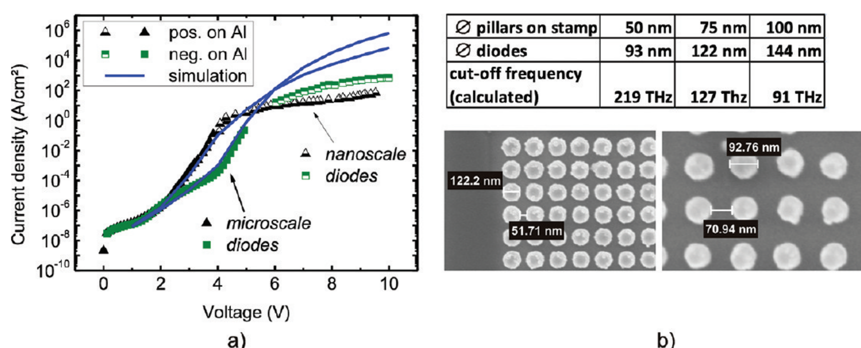

∅ pillars on stamp	50 nm	75 nm	100 nm
∅ diodes	93 nm	122 nm	144 nm
cut-off frequency (calculated)	219 THz	127 Thz	91 THz

Figure 4. *I*−*V* Characteristics of MIM nanodiode. (a) The *I*−*V* characteristic of a transfer-printed nanoscale MIM pillar (half-open symbols), measured using a conductive AFM setup, is presented in comparison with previously fabricated microscale MIM diodes (full symbols), characterized with a probe station, and numerical simulations (line). For a better comparison the positive and the negative polarity (on aluminum) are both shown on the positive *V*-axis, and the absolute logarithmic scale is used for the current density for the same reason. The nanoscale and microscale MIM structures show an excellent agreement, and the simulation could extract static device parameters. (b) The calculated cutoff frequencies of three different transfer-printed MIM diodes comprising areas between 93 and 144 nm are shown in the table, and two SEM images show the spatial dimensions of MIM diode arrays.

in a low noise probe station and the diodes showed a capacitance density of $C/A = 1.19 \times 10^{-6}$ F/cm^2.[31]

We showed that the dielectric constant ε_r is strongly dependent on the insulator thickness, although it is independent of the area *A*. The resistance *R* of the AuPd substrate that took over the lead lines was determined to be 8.93 Ω. The area of the MIM tunneling diodes was measured *via* SEM, and the diameter of the smallest printed pillars was determined to be 93 nm. A cut-frequency of 219 THz for the smallest MIM diodes can therefore be estimated. A further increase of the cutoff frequency is possible by reducing the diode area; however, because of the vertical thickness of the MIM nanodiodes, scaling down below 50 nm appears to be challenging so far. A better way to improve the performance of the device is the use of a low-k material, for example, with a permittivity below the value of 4.8 that we determined for the 3.6 nm thin AlOx.

CONCLUSION

We have presented a sophisticated large-area nanoscale device fabrication method for the transfer-printing of metal−oxide−metal tunneling nanodiodes which feature asymmetric *I*−*V* characteristics. We showed that the efficient fabrication of several million tunneling nanodiodes within one process step is possible. An implementation to CMOS technology can realistically be considered, as the transfer-printing process is applicable for almost every substrate and the temperature required is rather low. We can tailor the cutoff frequency by varying the diode area, as the general conducting mechanism and the static device parameters are independent of the diode area. The AlOx insulator has a thickness of 3.6 nm and retains its high quality during the printing process, so that even voltages up to 10 V can be applied without destroying the quantum device. The electrical performance of the nanoscale devices is in good agreement

with previously fabricated microdiodes. Numerical simulation shows that direct Fowler–Nordheim tunneling is the main conducting mechanism for the electrons, and static device parameters were extracted. Since the cutoff frequency of the smallest diodes is estimated as 219 THz, MIM nanodiodes are promising for extremely high-speed electronic and optoelectronic applications. Moreover, the fabrication of these nanoscale devices in dense arrays over large areas provides the possibility to fabricate terahertz rectifiers or also other devices in an economic and fast way.

METHODS

Hydrophobization of the Stamp. The silicon stamp was cleaned and activated by exposing it for 30 s to an oxygen plasma and then placed along with 0.5 mL of 1*H*,1*H*,2*H*,2*H*-perflouroctyltrichlorosilane (Alfa Aesar, Ward Hill, USA) into a desiccator at a pressure of 10 mbar for 15 min. This results in the formation of a hydrophobic self-assembled monolayer (SAM) on the surface of the stamp. The SAM was annealed by placing the stamp on a hot plate at a temperature 140 °C for 30 min.

Metal Deposition onto the Stamp. A stack of AuPd (15 nm thick) and Ti (4 nm thick) was deposited onto the SAM-covered silicon stamp in a Leybold UNIVEX 450 vacuum evaporator. To minimize the amount of metal deposited onto the sidewalls of the pillars, collimator plates with an aperture diameter of 5 cm were placed over the evaporation sources, and the substrate was placed at a relatively long distance of about 30 cm from the sources. The background pressure during the evaporations was below 10^{-6} mbar and the deposition rate was 0.4 Å/s. Following the deposition of the AuPd/Ti stack, a 25 nm thick Al layer was deposited in a Leybold UNIVEX 300 vacuum evaporator at a background pressure of about 10^{-7} mbar.

Insulator Growth on the Stamp. The AlOx insulator was obtained by oxidizing the surface of the 25 nm thick Al layer in an Oxford Plasma Technology reactive ion etch (RIE) system operated at an oxygen pressure of 10 mTorr and with a plasma power of 200 W for 30 s. This results in the formation of a dense, 3.6 nm thick AlOx insulator.

Metal Deposition onto the Target Substrate. As the target substrate, a doped silicon wafer was employed. A stack of Ti (4 nm thick), AuPd (25 nm thick), and Ti (4 nm thick) was deposited onto the wafer in a Leybold UNIVEX 350G vacuum evaporator. The background pressure during the evaporations was 2.5×10^{-6} mbar and the deposition rate was 0.4 Å/s. To obtain a uniform film thickness, the wafer was rotated during the evaporations.

Transfer Printing of MIM Nanodiodes. The Ti layers on the surfaces of the stamp and the target wafer were activated (hydophilized) by exposing them to an oxygen plasma for 10 s (stamp) and 2 min (wafer) in a microwave plasma generator operated at an oxygen flow rate of 80 mL/min and with a plasma power of 200 W. The stamp and the substrate were then placed in an Obducat NIL 2.5 nanoimprinter, heated to a temperature of 200 °C, and then pressed against each other for 3 min with a pressure of 50 bar. After allowing the stamp and the substrate to cool to a temperature of 90 °C, the stamp was released, thus transferring the MIM nanodiodes to the target substrate.

Electrical Characterization of MIM Nanodiodes. We used an Asylum Research MFP-3D atomic force microscope with an ORCA holder that features two transimpedance amplifiers with a gain of either 1×10^{6} V/A or 1×10^{9} V/A. The sample was clamped *via* the conductive substrate to a gold electrode, which was also connected to the cantilever holder (head), thus creating a complete circuit between the sample and the cantilever tip. We used Ti/Pt (5/20)-coated silicon tips (OMCL-AC240TM, Olympus, Japan) for the measurement. More details on these measurements can be found in the Supporting Information.

Conflict of Interest: The authors declare no competing financial interest.

Acknowledgment. The authors thank Tatyana Orlova at the Notre Dame Integrated Imaging Facility (NDIIF) for her invaluable help and IMS Chips for their support. The research leading to these results has received funding from the Institute for Advanced Study (IAS), the International Graduate School for Science and Engineering (IGSSE) at the Technische Universität München, the European Community's Seventh Framework Programme (FP7/2007-2013) under Grant Agreement No. 228673, the NSF through Grant CCF-1129098, and the German Excellence Cluster 'Nanosystems Initiative Munich' (NIM).

Supporting Information Available: Theoretical and experimental sections including five figures: S1, theoretical background of metal–insulator–metal diodes; S2, nanotransfer technology; S3, measurement setup for conductive AFM tips; S4, simulation; S5, air-oxidized MIM diodes. This material is available free of charge *via* the Internet at http://pubs.acs.org.

REFERENCES AND NOTES

1. Novotny, L.; van Hulst, N. Antennas for Light. *Nat. Photon.* **2011**, *5*, 83–90.
2. Grover, S.; Moddel, G. Engineering the Current–Voltage Characteristics of Metal–Insulator–Metal Diodes Using Double-Insulator Tunnel Barriers. *Solid-State Electron.* **2012**, *67*, 94–99.
3. Gómez-Pedrero, J. A.; Ginn, J.; Alda, J.; Boreman, G. Modulation Transfer Function for Infrared Reflectarrays. *Appl. Opt.* **2011**, *50*, 5344–5350.
4. Hongzhong, L.; Bangdao, C.; Xin, L.; Weihua, L.; Yucheng, D.; Bingheng, L. A Metal/Insulator/Metal Field-Emission Cannon. *Nanotechnol.* **2011**, *22*, 455302.
5. Waser, R.; Aono, M. Nanoionics-Based Resistive Switching Memories. *Nat. Mater.* **2007**, *6*, 833–840.
6. Gatti, D.; Gambetta, A.; Castrillo, A.; Galzerano, G.; Laporta, P.; Gianfrani, L.; Marangoni, M. High-Precision Molecular Interrogation by Direct Referencing of a Quantum-Cascade-Laser to a Near-Infrared Frequency Comb. *Opt. Express* **2011**, *19*, 17520–17527.
7. Walters, R. J.; van Loon, R. V. A.; Brunets, I.; Schmitz, J.; Polman, A. A Silicon-Based Electrical Source of Surface Plasmon Polaritons. *Nat. Mater.* **2010**, *9*, 21–25.
8. Ferguson, B.; Zhang, X.-C. Materials for Terahertz Science and Technology. *Nat. Mater.* **2002**, *1*, 26–33.
9. Grossman, M.; Born, B.; Heyden, M.; Tworowski, D.; Fields, G. B.; Sagi, I.; Havenith, M. Correlated Structural Kinetics and Retarded Solvent Dynamics at the Metalloprotease Active Site. *Nature Struct. Mol. Biol.* **2011**, *18*, 1102–1108.
10. Jegert, G.; Kersch, A.; Weinreich, W.; Lugli, P. Monte Carlo Simulation of Leakage Currents in TiN/ZrO_2/TiN Capacitors. *IEEE Trans. Electron Devices* **2011**, *58*, 327–334.
11. Bean, J. A.; Tiwari, B.; Bernstein, G. H.; Fay, P.; Porod, W. Thermal Infrared Detection Using Dipole Antenna-Coupled Metal-Oxide-Metal Diodes. *J. Vac. Sci. Technol., B* **2009**, *27*, 11–14.
12. Midrio, M.; Romagnoli, M.; Boscolo, S.; De Angelis, C.; Locatelli, A.; Modotto, D.; Capobianco, A. Flared Monopole Antennas for 10μm Radiation. *IEEE J. Quantum Electron.* **2011**, *47*, 84–91.
13. Periasamy, P.; Berry, J. J.; Dameron, A. A.; Bergeson, J. D.; Ginley, D. S.; O'Hayre, R. P.; Parilla, P. A. Fabrication and Characterization of MIM Diodes Based on Nb/Nb_2O_5 *via* a Rapid Screening Technique. *Adv. Mater.* **2011**, *23*, 3080–3085.
14. Bean, J. A.; Weeks, A.; Boreman, G. D. Performance Optimization of Antenna-Coupled Al/AlOx/Pt Tunnel Diode

Infrared Detectors. *IEEE J. Quantum Electron.* **2011**, *47*, 126–135.

15. Alda, J.; Rico-García, J. M.; López-Alonso, J. M.; Boreman, G. Optical Antennas for Nano-Photonic Applications. *Nanotechnol.* **2005**, *16*, S230–S264.
16. Grover, S.; Model, G. Applicability of Metal/Insulator/Metal (MIM) Diodes to Solar Rectennas. *IEEE J. Photovoltaics* **2011**, *1*, 78–82.
17. Tiwari, B.; Bean, J. A.; Szakmany, G.; Bernstein, G. H.; Fay, P.; Porod, W. Controlled Etching and Regrowth of Tunnel Oxide for Antenna-Coupled Metal–Oxide–Metal Diodes. *J. Vac. Sci. Technol., B* **2009**, *27*, 2153–2160.
18. Meitl, M. A.; Zhu, Z.-T.; Kumar, V.; Lee, K. J.; Feng, X.; Huang, Y. Y.; Adesida, I.; Nuzzo, R. G.; Rogers, J. A. Transfer Printing by Kinetic Control of Adhesion to an Elastomeric Stamp. *Nat. Mater.* **2006**, *5*, 33–38.
19. Chanda, D.; Shigeta, K.; Gupta, S.; Cain, T.; Carlson, A.; Mihi, A.; Baca, A. J.; Bogart, G. R.; Braun, P.; Rogers, J. A. Large-Area Flexible 3D Optical Negative Index Metamaterial Formed by Nanotransfer Printing. *Nat. Nanotechnol.* **2011**, *6*, 402–407.
20. Kim, T.-H.; Cho, K.-S.; Lee, E. K.; Lee, S. J.; Chae, J.; Kim, J. W.; Kim, D. H.; Kwon, J.-Y.; Amaratunga, G.; Lee, S. Y.; *et al.* Full-Colour Quantum Dot Displays Fabricated by Transfer Printing. *Nat. Photon.* **2011**, *5*, 176–182.
21. Li, D.; Guo, L. J. Organic Thin Film Transistors and Polymer Light Emitting Diodes Patterned by Polymer Inking and Stamping. *J. Phys. D: Appl. Phys.* **2008**, *41*, 105115.
22. Bareiß, M.; Tiwari, B. N.; Hochmeister, A.; Jegert, G.; Zschieschang, U.; Klauk, H.; Fabel, B.; Scarpa, G.; Koblmüller, G.; Bernstein, G. H.; *et al.* Nano Antenna Array for Terahertz Detection. *IEEE Trans. Microwave Theory Tech.* **2011**, *59*, 2751–2757.
23. Yuan, Y.; Reece, T. J.; Sharma, P.; Poddar, S.; Ducharme, S.; Gruverman, A.; Yang, Y.; Huang, J. Efficiency Enhancement in Organic Solar Cells with Ferroelectric Polymers. *Nat. Mater.* **2011**, *10*, 296–302.
24. Bartsch, S. T.; Lovera, A.; Grogg, D.; Ionescu, A. M. Nanomechanical Silicon Resonators with Intrinsic Tunable Gain and Sub-nW Power Consumption. *ACS Nano* **2012**, *6*, 256–264.
25. Kim, C.; Prada, M.; Blick, R. H. Coulomb Blockade in a Coupled Nanomechanical Electron Shuttle. *ACS Nano* **2012**, *6*, 651–655.
26. Loo, Y.-L.; Lang, D. V.; Rogers, J. A.; Hsu, J. W. P. Electrical Contacts to Molecular Layers by Nanotransfer Printing. *Nano Lett.* **2003**, *3*, 913–917.
27. Sekitani, T.; Zschieschang, U.; Klauk, H.; Someya, T. Flexible Organic Transistors and Circuits with Extreme Bending Stability. *Nat. Mater.* **2010**, *9*, 1015–1022.
28. Bareiß, M.; Imtaar, M. A.; Fabel, B.; Scarpa, G.; Lugli, P. Temperature Enhanced Large Area Nano Transfer Printing on Si/SiO_2 Substrates Using Si Wafer Stamps. *J. Adhes.* **2011**, *87*, 893–901.
29. Kamat, P. V. Quantum Dot Solar Cells. Semiconductor Nanocrystals as Light Harvesters. *J. Phys. Chem. C* **2008**, *112*, 18737–18753.
30. Sung, M. G.; Lee, H.; Heo, K.; Byun, K.-E.; Kim, T.; Seo, D. H.; Seo, S.; Hong, S. Scanning Noise Microscopy on Graphene Devices. *ACS Nano* **2011**, *5*, 8620–8628.
31. Bareiß, M.; Hochmeister, A.; Jegert, G.; Zschieschang, U.; Klauk, H.; Huber, R.; Grundler, D.; Porod, W.; Fabel, B.; Scarpa, G.; *et al.* Printed Array of Thin-Dielectric Metal–Oxide–Metal (MOM) Tunneling Diodes. *J. Appl. Phys.* **2011**, *110*, 044316.
32. Jirauschek, C. Accuracy of Transfer Matrix Approaches for Solving the Effective Mass Schrödinger Equation. *IEEE J. Quantum Electron.* **2009**, *45*, 1059–1067.
33. Jegert, G.; Kersch, A.; Weinreich, W.; Schroder, U.; Lugli, P. Modeling of Leakage Currents in High-Kappa Dielectrics: Three-Dimensional Approach *via* Kinetic Monte Carlo. *Appl. Phys. Lett.* **2010**, *96*, 062113.
34. Robertson, J. Band Offsets of Wide-Band-Gap Oxides and Implications for Future Electronic Devices. *J. Vac. Sci. Technol., B* **2000**, *18*, 1785–1791.
35. Robertson, J. Band Offsets and Work Function Control in Field Effect Transistors. *J. Vac. Sci. Technol., B* **2009**, *27*, 277–285.
36. Wingreen, N. S.; Jacobsen, K. W.; Wilkins, J. W. Resonant Tunneling with Electron-Phonon Interaction: An Exactly Solvable Model. *Phys. Rev. Lett.* **1988**, *61*, 1396–1399.
37. Baierl, D.; Fabel, B.; Lugli, P.; Scarpa, G. Efficient Indium–Tin–Oxide (ITO) Free Top-Absorbing Organic Photodetector with Highly Transparent Polymer Top Electrode. *Org. Electron.* **2011**, *12*, 1669–1673.

High-Yield Transfer Printing of Metal-Insulator-Metal Nanodiodes

Mario Bareiß, Frederik Ante, Daniel Kälblein, Gunther Jegert, Christian Jirauschek, Giuseppe Scarpa, Bernhard Fabel, Edward M. Nelson, Gregory Timp, Ute Zschieschang, Hagen Klauk, Wolfgang Porod, and Paolo Lugli*

The supplementary information contains support of the main manuscript. Text and five figures discuss five specific topics:

1. Theoretical background of MIM diodes
2. Nano transfer printing technology
3. Measurement setup for conductive AFM tips
4. Simulation
5. Air-oxidized MIM diodes

S1. Theoretical background of metal-insulator-metal diodes

A metal-insulator metal (MIM) diode consists of two metal plates that are arranged parallel to each other and features a thin dielectric between this metal plates, to guarantee a sufficient probability for charge carriers to tunnel from one metal in the other one.[1] As the tunneling current I_t is dependent exponentially[2] of the voltage V, the amount of tunneling electrons with respect to the polarity of the electron flux is different when an alternating field is applied on the MIM structure under an external bias.[3] For example, when a constant voltage of 2 V is applied to one metal with respect to the other one and in addition to that, an AC field of 100 mV is applied, more electrons are tunneling from the electrode that is positive biased (DC) to the electrode that is negative biased (DC) than the other way and thus, a direct current is formed. The conversion from AC to DC is more efficient when a larger voltage is applied because of the exponential I_t-V-characteristics, therefore, *e.g.* for detecting devices, MIM diodes with large break-down voltages are desirable. So far, this is correct when the two electrodes consist of metals with similar or dissimilar work functions. When fabricating MIM diodes containing work functions with dissimilar metal electrodes like gold as the first electrode and aluminum as a second electrode, an asymmetric slope of the I_t-V-characteristics is even achieved when no biased is applied to the junction.[4] In such a structure, the electrons have a higher effective energy barrier when tunneling from the high work function material to the low one than in the other way. Thus, an effective direct current I_t from the low work function material to the high work function material occurs.

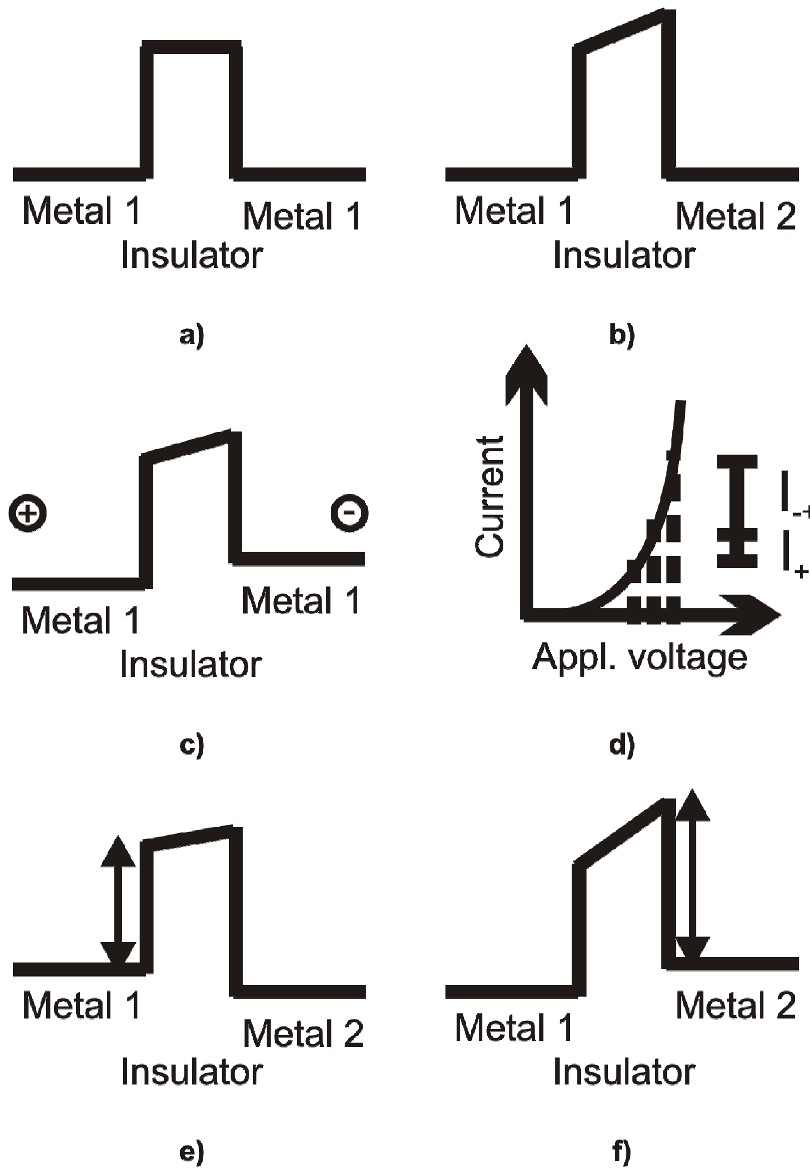

Figure S1: The band structure of a MIM diode a) with similar metals and b) metals with dissimilar work functions is shown in steady state. When a voltage is applied on an electrode of the similar or dissimilar MIM diode, c) the Fermi-levels of the metals are not aligned anymore and an electrical current occurs. d) An AC signal that is applied in addition to the external bias (DC), displaces electrons from the cathode to the anode (I_{-+}) and the other way (I_{+-}) with the frequency of the AC signal. However, as the I-V-characteristics are exponential, the resulting direct current which is the difference between I_{-+} and I_{+-} is directed from the cathode to the anode. This asymmetric current is also achievable without an external bias when two metals with dissimilar work functions are used. When a surplus of electrons is formed in e) metal 1, the tunnel barrier for the electrons is lower than when a surplus of electrons is formed in f) metal 2 which results in an asymmetric current around zero volts.

S2. Nanotransfer printing technology

In the nanotransfer printing process, a Si wafer featuring *e.g.* pillars, covered with a hydrophobic organic self-assembled monolayer (SAM) of perflouroctyltrichlorsilane[5] for providing weak adhesion between the surface of the stamp and materials that are deposited thereon, is used as a stamp. The process steps for the formation of the SAM on the Si wafer are briefly presented:

1. Exposing the Si wafer to an oxygen plasma for 30 s to create a high density of hydroxyl groups (hydrophilic) for molecular self-assembly
2. Placing the activated Si wafer together with 0.5 ml of the SAM in a vacuum chamber at a pressure of 10 mbar for 15 min for SAM formation on the Si surface
3. Annealing of Si wafer comprising hydrophobic SAM at 140°C for 30 min for enhancing the assembly of the molecules on the surface.

The silane-based SAM provides a strong physical resistance and temperatures around 500°C[6] do not change its performance. Thus, metals can be deposited on the Si wafer by thermal evaporation without destroying the SAM. The first layer that is deposited is preferably a noble metal, like Au, Pt or AuPd. As noble metals provide weak adhesion to almost any surfaces, the metal can be detached from the stamp easily. Here, AuPd has been chosen for providing also a smooth surface. The subsequent process steps are presented here:

1. Deposition of 15 nm AuPd for providing a weak adhesion to the stamp.
2. Deposition of 25 nm Al as a first metal electrode.
3. Plasma treatment of naturally formed aluminum oxide: Oxygen plasma at 200 W for 30 s. A compact AlO_x layer is formed comprising a thickness of 3.6 nm.[7]
4. Deposition of 20 nm AuPd and 4 nm Ti as the second metal electrode and as an adhesion promoter, respectively between the material stack from the stamp and the target substrate.

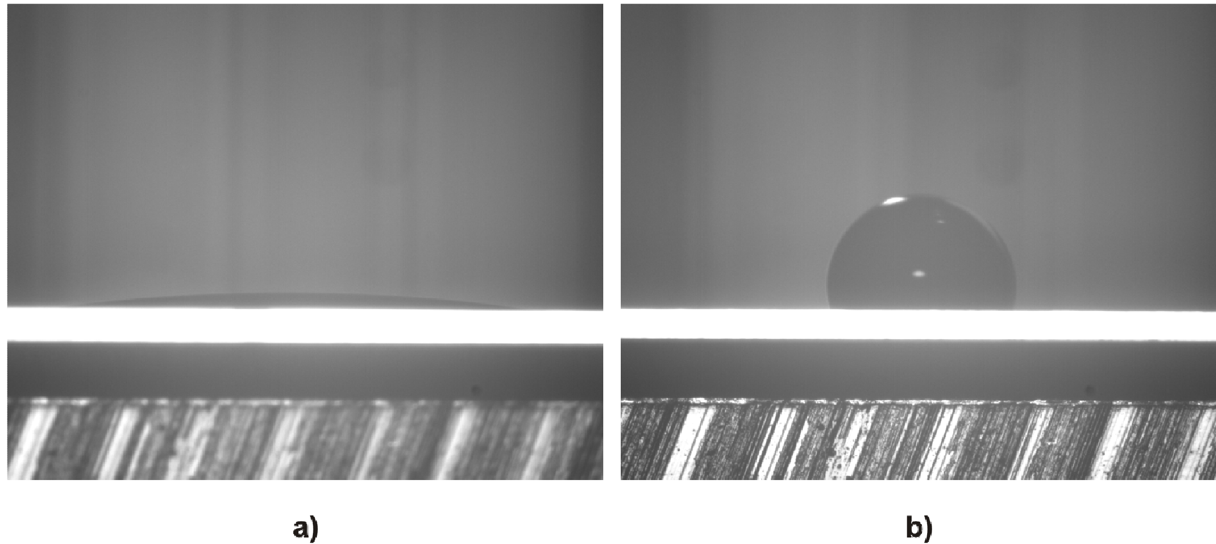

Figure S2: Surface energy is adjustable by a) a plasma treatment in order to from hydrophilic silanol groups on the Si wafer, or b) by saturating open bonds on the surface with a hydrophobic organic self-assembled monolayer.

The substrate consists of a Si wafer that comprises a 30 nm thick layer of AuPd for contacting the bottom of the MIM diode. For providing a better adhesion, Ti is used as an adhesion promoter to the Si substrate as well as to the transferred material stack on the surface which is activated by brief plasma to achieve a hydrophilic surface. When the stamp is brought into contact with the substrate, only the elevated pillars on the stamp get into contact with the smooth surface of the substrate. Therefore, individual and separated vertical MIM nanodiodes are transferred to the substrate. The nanotransfer process was performed in a NIL 2.5 Nanoimprinter from the company Obducat at a temperature of 200°C and a pressure of 50 bar for 5 min. During the transfer process, the titanol surface groups on the stamp and on the substrate react to TiO_2 under water release. As this reaction is reversible, the transfer yield is strongly improved when applying temperatures above 150°C or applying vacuum conditions to release physisorbed water.[8] After removing the stamp from the substrate, the material stacks are transferred and the stamp can be used again.

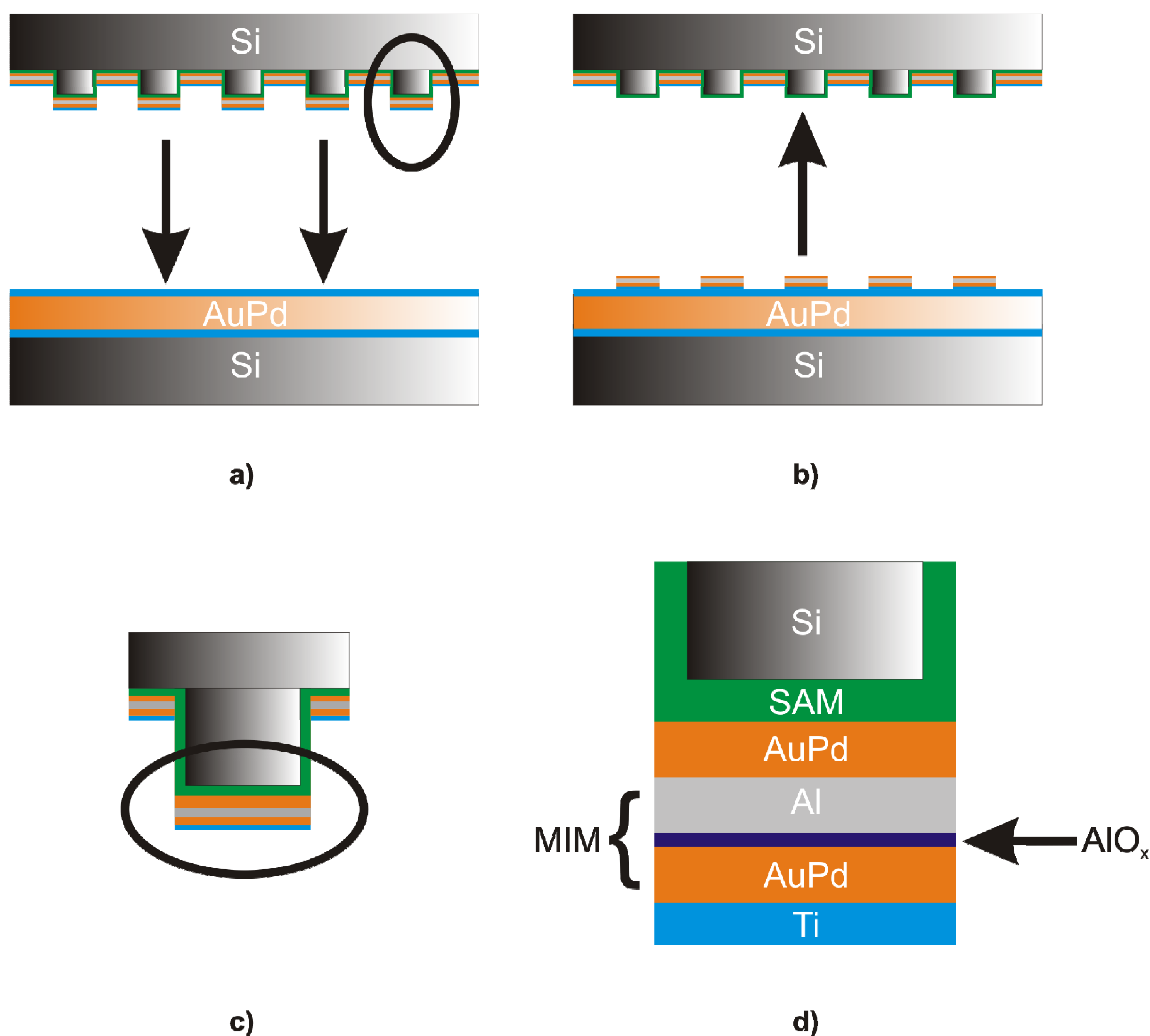

Figure S3: The nanotransfer printing process is shown in detail. a) Before the transfer process, the Si wafer stamp is covered with an organic self-assembled monolayer (green). The AuPd layer (orange) attached to the SAM layer provides weak adhesion between the MIM diode and the stamp. The Al layer (gray) serves as the first metal electrode. Then, the stamp is treated with a brief oxygen plasma exposure to form an AlO_x dielectric (violet). The second electrode is AuPd. The last layer is Ti (blue) that is an adhesion promoter between the MIM diode and the target substrate. When the stamp comprising the metals and the dielectric is brought into physical contact with the substrate which is covered with a AuPd layer (orange) and two Ti layers (blue) for providing a good adhesion, b) the material stack on the elevated structures is transferred to the substrate. The SAM remains on the stamp and can be used again. In c), a zoom of the structures on the stamp (black circle in Figure S3a)) is shown. In d), the material stacks on the stamp are shown in detail (black circle in Figure S3c)).

S3. Measurement setup for conductive AFM tips

The IV characteristic of the MIM device was measured by conductive atomic force microscopy (AFM). We used an MFP-3D AFM (Asylum Research, California) with an ORCA holder that features two transimpedance amplifiers with a gain of either $1x10^6$ V/A or $1x10^9$ V/A. The sample was clamped *via* the conductive substrate to a gold electrode, which was also connected to the cantilever holder, thus creating a complete circuit between the sample and the cantilever tip. We used Ti/Pt (5/20) coated silicon tips (OMCL-AC240TM, Olympus, Japan) for the measurement.

First, the topography of the sample was measured in AC tapping mode. Then, after a target structure was identified, the AFM cantilever tip was brought into direct contact with the surface. To ensure a good electrical connection, the tip was dithered in an outwardly expanding 5 nm spiral pattern in a span of 5 seconds. Then, the tip was held motionless as an electrical bias was applied through a cyclic, triangle wave pattern, to the sample through the gold electrodes on the sample mount while the current was simultaneously measured at the tip. This was repeated numerous times at different locations on the MIM device.

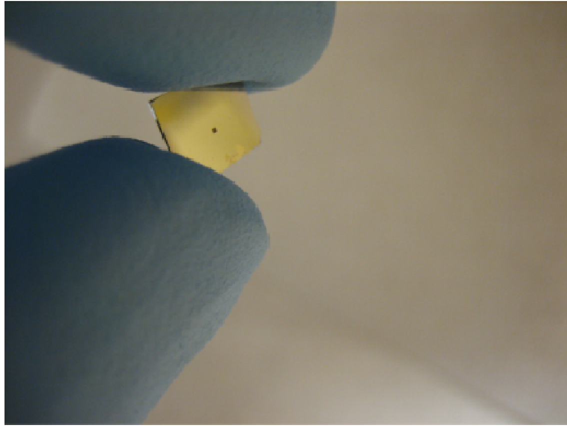

a)

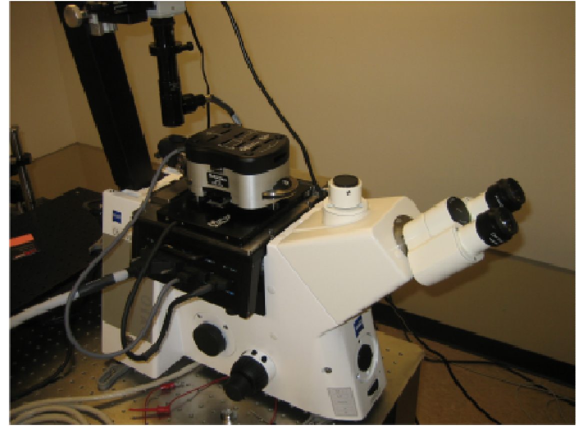

b)

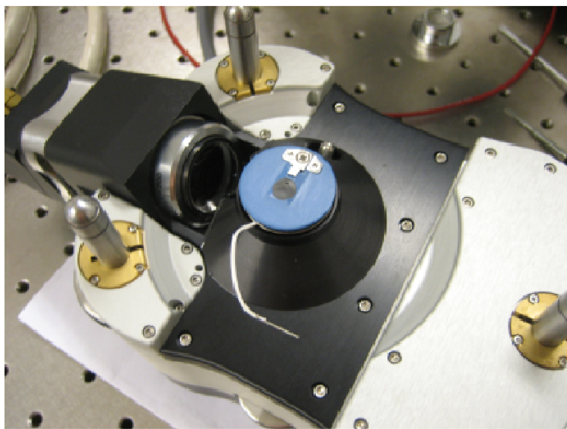

c)

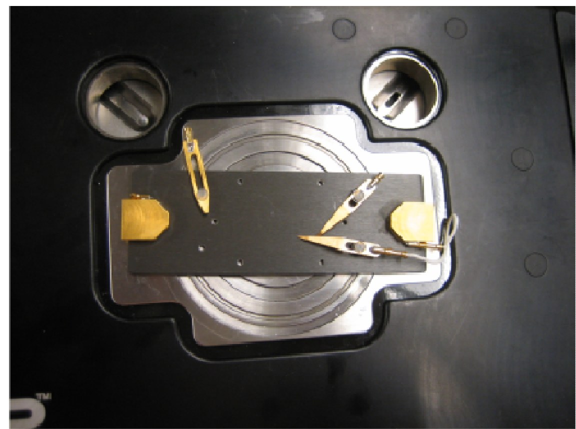

d)

Figure S4: a) The substrate containing the array of transfer-printed MIM nanodiodes is shown here. The structures in the center of the substrate represent the MIM diode array. b) The MIM diodes were electrically characterized by a conductive AFM setup. The head after 180° rotation is shown in c). The conductive AFM tip is placed in the center of the blue area and is connected to the white cable. d) The substrate containing the tunneling nanodiodes is placed on a ceramic holder comprising gold clamps for contacting the conductive surface. The end of the white cable shown in c) is during the measurement placed on the right gold pad in d) and thus, and circuit is closed.

S4. Simulation

The simulation is based on the numerical evaluation of the Tsu-Esaki formula[9] for the current density

$$J = \frac{e m_e k_B T}{2\pi^2 \hbar^3} \int P(E) \ln \left\{ \frac{1+\exp(-E/k_B T)}{1+\exp\left[-(eV+E)/k_B T\right]} \right\} \mathrm{d}E, \tag{1}$$

with the electron mass m_e, elementary charge e, Boltzmann constant k_B, reduced Planck constant $\hbar$, applied bias V, and temperature $T = 300$ K. The tunneling probability $P(E)$ for the electrons as a function of their energy E is computed using a transfer matrix formalism[10]. Tunnel barriers of 4.2 eV for the AuPd electrode and 2.8 eV for the Al electrode are assumed[11]. Nonparabolicity effects are implemented by using an energy dependent effective tunneling mass $m^*(E)$,[11,12] which contains the value $m^*(E=0)$ at the conduction band edge of the tunneling barrier as adjustable parameter; the best agreement with the experimental data in the low bias regime is obtained by setting $m^*(0) = 0.45\ m_e$.

S5. Air-oxidized metal-oxide-metal diodes

Our oxygen-plasma-grown AlOx tunnel barriers have a thickness of 3.6 nm. Insulators with even smaller thickness can in principle be obtained by simply allowing the surface of a reactive metal, such as Al, Ti or Cu, to spontaneously oxidize in ambient air.[13-15] Such thin barriers are expected to produce very large tunneling currents and therefore greater signal-to-noise ratio (in detectors) or larger energy efficiency (in photovoltaics). To explore this opportunity we also fabricated transfer-printed MIM diodes with an AlOx tunnel barrier produced simply by air exposure of the Al bottom electrode. The transfer yield for these diodes was 99.89 % (i.e., only one diode was not successfully transferred), and the current-voltage characteristics of these diodes were measured using a probe station and a parameter analyzer. We found that about 90% of the diodes with the naturally grown AlOx tunnel barrier showed short-circuit behavior, apparently due to direct contact between the top and bottom metal electrodes through the naturally grown AlOx tunnel barrier. The current-voltage characteristics of the remaining 10% of the diodes showed extremely large device-to-device variations, suggesting that the thickness of the naturally grown tunnel barrier was different in each device. By fitting kinetic Monte Carlo simulations to the experimental data[16,17] we have shown that the thickness of the naturally grown AlOx is very inhomogeneous across the diode array and that the AlOx thickness varied from less than 2.5 nm to about 3.6 nm. We did not find any diodes with an insulator thickness greater than 3.6 nm, which happens to be the thickness of the oxygen-plasma-grown AlOx tunnel barriers (see Figure S5). We therefore conclude that this thickness of 3.6 nm is the maximum AlOx thickness that is produced either by natural oxidation of aluminum in ambient air (although not homogenously across a large area) or by plasma oxidation of aluminum with a plasma power of 200 W (with excellent uniformity across large areas). Unlike the MIM diodes with the naturally grown AlOx tunnel

barrier, which are neither reliable nor reproducible, the MIM diodes with the oxygen-plasma-grown AlOx tunnel barrier show excellent reproducibility.

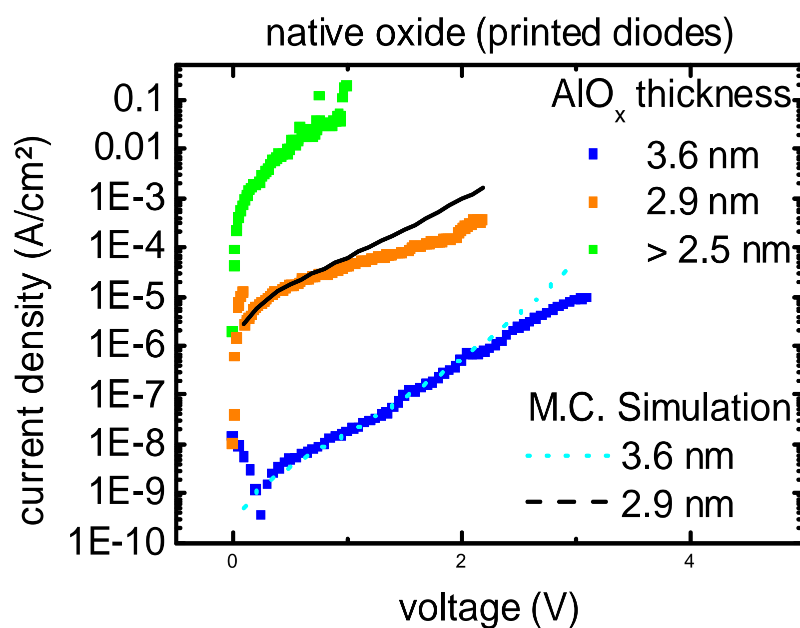

Figure S5: I-V- characteristics of printed MIM tunneling diodes featuring a naturally grown aluminum oxide as insulating material. The positive bias on Au is different for all three diodes, and the Monte Carlo simulation confirms that the thickness of the insulator is different in the three diodes, despite the same exposure time to air.

Supplementary References

1 Simmons, J. G. Generalized Formula for the Electric Tunnel Effect between Similar Electrodes Separated by a Thin Insulating Film. *J. Appl. Phys.* **1963,** *34*, 1793-1803.

2 Fowler, R. H.; Nordheim, L. Electron Emission in Intense Electric Fields. *Proceedings of the Royal Society of London. Series A, Mathematical and Physical Sciences* **1928,** *119*, 173-181.

3 Slovick, B. A.; Bean, J. A.; Krenz, P. M.; Boreman, G. D. Directional Control of Infrared Antenna-coupled Tunnel Diodes. *Opt. Express* **2010,** *18*, 20960-20967.

4 Bareiß, M.; Tiwari, B. N.; Hochmeister, A.; Jegert, G.; Zschieschang, U.; Klauk, H.; Fabel, B.; Scarpa, G.; Koblmüller, G.; Bernstein, G. H.; *et al*. Nano Antenna Array for Terahertz Detection. *IEEE Trans. Microwave Theory Tech.* **2011,** *59*, 2751-2757.

5 Kulinich, S. A.; Farzaneh, M. Hydrophobic Properties of Surfaces Coated with Fluoroalkylsiloxane and Alkylsiloxane Monolayers. *Surf. Sci.* **2004,** *573*, 379-390.

6 Okada, M.; Iwasa, M.; Nakamatsu, K.-i.; Kanda, K.; Haruyama, Y.; Matsui, S. Durability of Antisticking Layer Against Heat in Nanoimprinting Evaluated Using Scanning Probe Microscopy. *Microelectron. Eng.* **2009,** *86*, 657-660.

7 Klauk, H.; Zschieschang, U.; Pflaum, J.; Halik, M. Ultralow-Power Organic Complementary Circuits *Nature* **2007,** *445*, 745.

8 Bareiß, M.; Imtaar, M. A.; Fabel, B.; Scarpa, G.; Lugli, P. Temperature Enhanced Large Area Nano Transfer Printing on Si/SiO2 Substrates Using Si Wafer Stamps. *J. Adhes.* **2011,** *87*, 893-901.

9 Tsu, R.; Esaki, L. Tunneling in a Finite Superlattice. *Appl. Phys. Lett.* **1973,** *22*, 562-564.

10 Jirauschek, C. Accuracy of Transfer Matrix Approaches for Solving the Effective Mass Schrödinger Equation. *IEEE J. Quantum Electron.* **2009,** *45*, 1059-1067.

11 Bareiß, M.; Hochmeister, A.; Jegert, G.; Zschieschang, U.; Klauk, H.; Huber, R.; Grundler, D.; Porod, W.; Fabel, B.; Scarpa, G.; *et al*. Printed Array of Thin-Dielectric Metal-Oxide-Metal (MOM) Tunneling Diodes. *J. Appl. Phys.* **2011,** *110*, 044316.

12 Ekenberg, U. Nonbarabolicity Effects in a Quantum Well: Sublevel Shift, Parallel Mass, and Landau Levels. *Phys. Rev. B* **1989,** *40*, 7714-7726.

13 Periasamy, P.; Berry, J. J.; Dameron, A. A.; Bergeson, J. D.; Ginley, D. S.; O'Hayre, R. P.; Parilla, P. A. Fabrication and Characterization of MIM Diodes Based on Nb/Nb2O5 *via* a Rapid Screening Technique. *Adv. Mat.* **2011,** *23*, 3080-3085.

14 Bean, J. A.; Tiwari, B.; Bernstein, G. H.; Fay, P.; Porod, W. Thermal Infrared Detection Using Dipole Antenna-coupled Metal-Oxide-Metal Diodes. *J. Vac. Sci. Technol. B* **2009,** *27*, 11-14.

15 Zou, G.; Liu, R.; Chen, W.; Xu, Z. Preparation and Characterization of Lamellar-like Mg(OH)2 Nanostructures *via* Natural Oxidation of Mg Metal in Formamide/Water Mixture. *Mater. Res. Bull.* **2007,** *42*, 1153-1158.

16 Jegert, G.; Kersch, A.; Weinreich, W.; Schroder, U.; Lugli, P. Modeling of Leakage Currents in High-Kappa Dielectrics: Three-Dimensional Approach *via* Kinetic Monte Carlo. *Appl. Phys. Lett.* **2010,** *96*, 062113.

17 Jegert, G.; Kersch, A.; Weinreich, W.; Lugli, P. Monte Carlo Simulation of Leakage Currents in TiN/ZrO_2/TiN Capacitors. *IEEE Trans. Electron Devices* **2011,** *58*, 327-334.